

Formation and shrinkage of deposited track with varying powder layer thicknesses in selective laser melting process: multi-physics simulation

Patiparn Ninpetch¹ · Pruet Kowitwarangkul² · Prasert Chalermkarnnon³ · Kavin Karunratanakul³ · Kornrawee Munpakdee⁴ · Phadungsak Rattanadecho⁴

Received: 7 November 2024 / Revised: 17 July 2025 / Accepted: 19 July 2025 © The Author(s) under exclusive licence to OWZ 2025

Abstract

The selective laser melting (SLM) process has gained attention in the manufacturing industry due to its capability for producing products with complex shapes through a layer-by-layer addition. Selecting process parameters influences the as-built quality. Among these, the layer thickness and energy input are key parameters impacting the deposited track formation, shrinkage, and defects. This study implemented multi-physics simulation to examine deposited track formation with varying layer thicknesses (L_t) and linear energy density (LED) and investigate the process parameters impact on surface sinkage induced shrinkage of deposited track in the SLM process of Ti-6Al-4 V alloy. The results revealed that layer thickness significantly impacts temperature distribution, molten pool morphology, and surface sinkage of deposited track. With higher layer thicknesses the temperature distribution was transformed from V-shaped to U-shaped due to more uniform heat distribution. LED adjustments play an essential role in both formation and surface sinkage of deposited track. Lower LED at decreased layer thicknesses promotes uniform deposited tracks but can cause humping effect, while higher LED increased penetration depth at higher layer thickness but potential for keyholing and surface sinkage. These findings are expected to provide optimization of Ti-6Al-4 V production.

Keywords Selective laser melting process · Multi-physic simulation · Powder layer thickness · Formation and shrinkage of deposited track

1 Introduction

Selective laser melting (SLM) process has received significant attention as a manufacturing process for producing complex shape parts in automotive, aerospace, and medical industries [1]. The SLM process generally utilizes a high-power laser as heat source to melt and fuse the metal

- Pruet Kowitwarangkul
- Department of Industrial Engineering, Faculty of Engineering, Rajamangala University of Technology Thanyaburi, Pathum Thani 12110, Thailand

pruet.k@tggs.kmutnb.ac.th

Published online: 18 August 2025

- The Sirindhorn International Thai-German Graduate School of Engineering (TGGS), King Mongkut's University of Technology North Bangkok, Bangkok 10800, Thailand
- National Metal and Materials Technology Center, Pathum Thani 12120, Thailand
- Department of Mechanical Engineering, Faculty of Engineering, Thammasat University (Rangsit Campus), Pathum Thani 12121, Thailand

powder spread on substrate plate by means of a layer-bylayer additions [2, 3]. The operating parameters selection in the SLM process plays a vital role in controlling the quality, and mechanical properties of the build parts. The typical operating parameters include laser power (P), scanning speed (v), hatch spacing (H), layer thickness (L_t) , and energy input [4, 5]. Among these, the layer thickness is a key parameter in the SLM process, which has considerable impact on forming quality, and defect formation of final parts. Furthermore, this parameter influences the preparation efficiency, and building rate of the SLM process [6, 7]. Using high layer thickness is a capable method to raise the build rate, but it often leads to pore formation, poor roughness, and inferior mechanical properties of as-built part [8]. On the other hand, using a low layer thickness can ensure obtaining the parts with high density, and better surface quality. In general, the layer thickness in the SLM process range 20–60 µm [8]. However, employing the high layer thickness, it is imperative to determine appropriate process parameter, and energy input to achieve



production efficiency while ensuring the as-built quality. This is a significant issue and challenge in the SLM process.

For the SLM process, the initial layers thickness is set through the downward movement of the build platform along the Z-axis. Meanwhile, the thickness of further layer is different due to the shrinkage of deposited track after laser melting process [9, 10]. As a result, the actual thickness of further layer is combination between the distance movement of build platform in Z-direction, and the surface sinkage (S_s) of preceding deposited tracks [9]. The S_s is the distance between the top surface of powder bed to the top surface of deposited track morphology. Figure 1 shows schematic of the S_s induced by shrinkage of deposited track after the laser melting process. The shrinkage of deposited track significantly impacts on the dimensional accuracy of the final part. It is influenced by thermal gradients of the molten material and material properties. The S_s can essentially influence deposited track formation, overlap depth distance, and defects such as lack-of-fusion (LOF) in further layers. These factors are mainly affected by the energy input, namely, linear energy density (LED), which is defined as a ratio between laser power (P) and scanning speed (v) [11].

In addition to the prescribing of energy input, the formation, and shrinkage of deposited track are strongly influenced by the complex multi-physics phenomena that occur concurrently during building process. The phenomena include energy absorption, thermal-fluid behavior, phase transformation, and material vaporization [12, 13]. Nevertheless, it is quite challenging to observe the multi-physics phenomena through experimental studies because these typically take place at the micro-scale or meso-scale and transpire over a short period of time [12, 14]. To overcome, multi-physics modeling has become an effective alternative tool to investigate and gain a better understanding of the complicated physical phenomena as well as the impact of processing parameters on laser melting process, melting dynamics, and defects formation [15, 16]. To date, several researchers have attempted to develop a multi-physics simulation to explain the physical phenomena and examine the effects of process parameters on laser melting process, and defects formation during the SLM process [17, 18]. Panwisawas et al. [19] examined the influence of layer thickness and scanning speed on solidified track morphology using a numerical model. It was found that the solidified track has irregular shapes when high scanning speed and high layer thickness are utilized. Moreover, previous studies of multi-physics simulation in the SLM process of Ti-6Al-4 V alloy have been reviewed as shown in Table 1. The utilization of Ti-6Al-4 V alloy has gained significant popularity in the SLM process. This material offers low density, good corrosion resistance, and favorable biocompatibility properties [20, 21]. It provides a wide range of applications, including implantable medical devices, automobiles, and aerospace components [22].

As listed in Table 1, it was noticed that the number of studies developing and implementing multi-physics simulations to examine the formation of deposited tracks with varying layer thickness is notably limited.

Hence, this research aims to propose and implement multiphysics simulation to investigate formation of deposited track with varying layer thicknesses, and energy inputs during the SLM process of Ti-6Al-4 V alloy. In addition, the impact of process parameters on surface sinkage induced by shrinkage of deposited track were analyzed. Layer thickness and energy input variation for the study range from 30 to 90 μ m, and 100 to 213 J/m, respectively. The simulation was performed using the FLOW-3D AM software version 3.0, incorporating both a discrete element method (DEM) model and a computational fluid dynamics (CFD) model. The numerical results were validated against experimental findings as reported by Kouprianoff et al. [40]. The outcomes provide guidelines for the optimization of process parameters in the SLM of Ti-6Al-4 V.

2 Multi-physics modeling

The multi-physics simulation for SLM process generally includes two main processes, which are the powder bed preparation process, and laser melting process. The DEM model and CFD model were implemented to simulate the powder spreading, and the laser melting process. Figure 2 displays the procedure of multi-physics simulation for the SLM process.

2.1 Powder bed preparation model

The DEM model was applied to calculate and simulate the movement of particles such as particles to particles and particles to wall interactions for metal particle distribution on solid substate and packing. The metal particles were shaped into a spherical form with several radii. The individual powder velocities in x, y, and z directions were regarded by DEM model for solving Newton's second law of motion. The models of particle-to-particle can be described in Eqs. (1), (2) and (3): [41]

Particle interaction force in normal direction:

$$F_{ni} = -k_s d \ln -\eta_n (u' \cdot n) n \tag{1}$$

Particle interaction force in tangential direction:

$$F_{ti} = -\eta_t(u' - (u' \cdot n)n) \tag{2}$$



Fig. 1 Schematic of the surface sinkage (S_s) induced by the shrinkage of deposited track after melting process. (Color figure online)

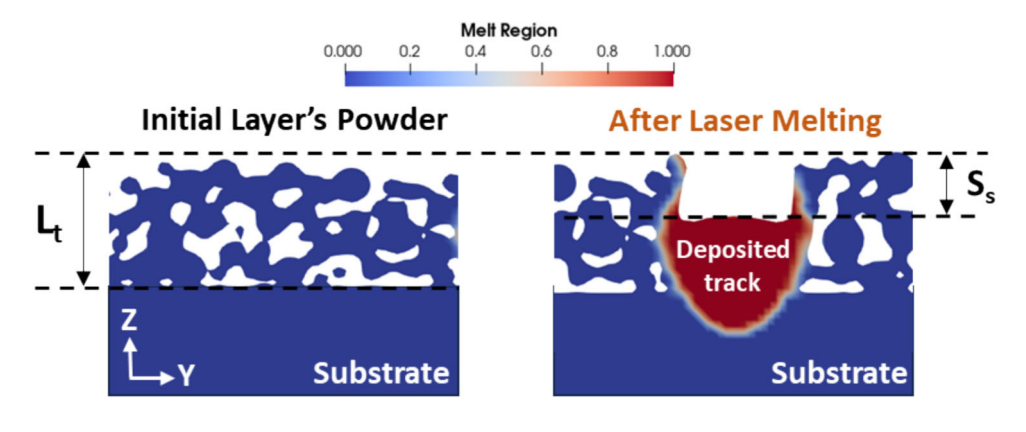
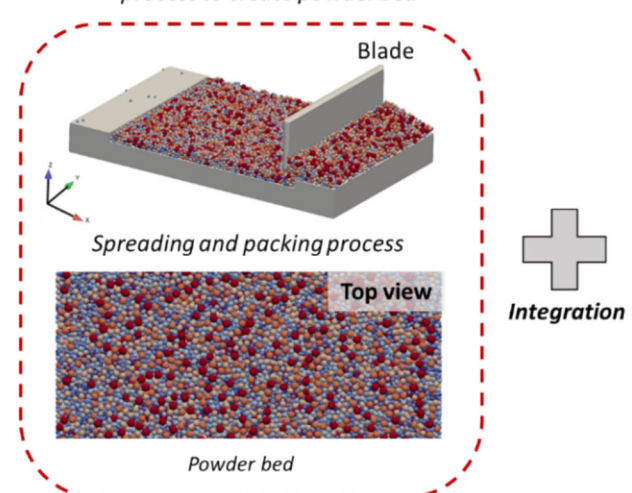


Table 1 Previous studies of multi-physics simulation in SLM process of Ti-6Al-4 V

Parameters varying to study the formation of deposited tracks						
Laser power	Scanning speed	Layer thickness	Other parameters			
[23–25] [26–30]	[19, 20, 23–29, 31, 32],	[19, 33–35]	[36–39]			

(a) **DEM model**: Powder bed preparation process

 Simulate powder spreading and packing process to create powder bed



(b) CFD model: Laser melting process

Simulate thermal behaviors, molten pool dynamics, and deposited track formation

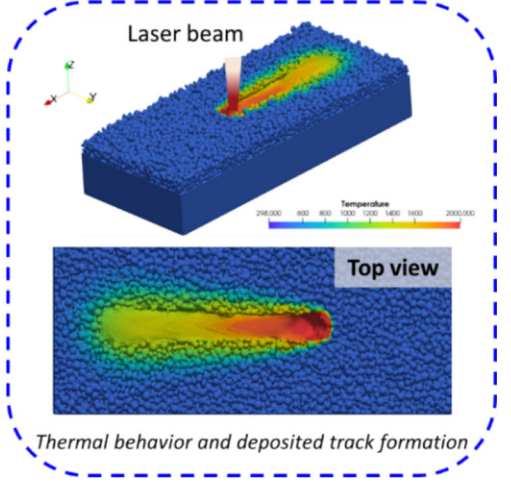


Fig. 2 Procedure of multi-physics simulation for SLM process. (Color figure online)

Total particle interaction force:

$$F_{i} = F_{ni} + F_{ti} = -F_{j}$$

$$l_{0} = r_{i} + r_{j}; l = X_{j} - X_{i}; dl = l_{0} - ||l||;$$

$$n = \frac{1}{l}; u' = u_{j} - u_{i}$$
(3)

where X_i , is a coordinate vector of an individual particle center, r is particle radius, k_s is spring constant, u is particle velocity vector, and η is drag coefficient. is normal vector.

2.2 Heat transfer and fluid dynamics model

During the laser-material interaction in SLM process, complex physical phenomena including heat transfer, fluid dynamics, and phase transformation of materials are associated. The governing equations, including mass, energy, and momentum conservations were applied to consider the heat transfers, fluid dynamics, and phase transformation in SLM process as described in Equations (4)-(6) [42, 43]. To simplify the numerical simulation, the fluid flow behavior of molten metal was assumed as laminar flow, and Newtonian fluid. To numerically consider the heat convection inside of



melt pool and Marangoni effect on the melt pool surface, the surface tension model was employed. The volume of fluid (VOF) model was also utilized to create molten pool surface morphology. The surface tension model with temperature dependent and VOF model are expressed in Equation (7) and (8) [44]:

$$\frac{\partial \rho}{\partial t} + \nabla \cdot (\rho \vec{v}) = 0 \tag{4}$$

$$\frac{\partial H}{\partial t} + (\vec{v}.\nabla)H = -\frac{1}{\rho}(\nabla .k\nabla T) + \dot{q}$$
 (5)

$$\frac{\partial \stackrel{\rightarrow}{v}}{\partial t} + \left(\vec{v}.\nabla\right)\vec{v} = -\frac{1}{\rho}\nabla P + \mu\nabla^2\stackrel{\rightarrow}{v} + \stackrel{\rightarrow}{g} + F_b \tag{6}$$

$$\gamma(T) = \gamma_o + \frac{d\gamma}{dT}(T - T_{\rm m}) \tag{7}$$

where \overrightarrow{v} is the molten metal velocity, P is the pressure, ρ is density, μ is kinetic viscosity, g is gravity force, F_b is the buoyancy force, H is enthalpy, k is thermal conductivity, T is temperature, \dot{q} is heat source term, and t is time, γ is the surface tension at temperature, γ_o is the surface tension at melting temperature, T_m is melting temperature, and $\frac{d\gamma}{dT}$ is surface tension coefficient with temperature dependent.

$$\frac{\partial F}{\partial t} + \nabla \cdot \left(\overrightarrow{vF} \right) = 0 \tag{8}$$

A cell is void when F = 0, and completely occupied by the fluid when F = 1. When the value of F is between 0 and 1, an interface between the fluid and void exists in the cell.

2.3 Material evaporation model

Equation (9) shows the recoil pressure, which was used to consider the gasification recoil force on the molten pool surface. The gasification recoil force occurs when the temperature at melt pool surface surpasses boiling temperature of material [45]:

$$P_r = 0.54 P_o \exp\left(\Delta H_{\rm v} \frac{T - T_{\rm b}}{RTT_{\rm b}}\right) \tag{9}$$

where P_0 is the saturation pressure, ΔH_v is the enthalpy of metal vapor, R is gas constant, and T_b is boiling temperature.

2.4 Moving laser heat source model

The SLM process commonly employs the moving laser heat source with high energy to fully melt the metal powders bed. Therefore, Gaussian laser heat source model was determined

Table 2 Thermal–physical properties of Ti-6Al-4 V used in the calculation [14, 48]

Material property	Value		
Solidus temperature (K)	1,873		
Liquidus temperature (K)	1,923		
Boiling temperature (K)	3,533		
Latent heat of fusion (J/kg)	2.9×10^{5}		
Latent heat of evaporation (J/kg)	8.3×10^{6}		

as a moving heat source over the powder layer as explained in Equation (10) [46, 47]:

$$Q = \frac{A_c P}{\pi r_s} exp \left(-2 \frac{(x - x_s)^2 + (y - y_s)^2}{r_s^2} \right)$$
 (10)

where Q is the surface heat flux, A_c is the absorption coefficient, P is the laser power, r_s is the laser radius, x_S and y_S are the coordinates of the laser beam center.

2.5 Simulation configuration, thermal-physical properties, and operating parameters

In this study, a multi-physics simulation has been conducted via FLOW-3D AM software version 3.0. The simulation setup process began with the utilization of the DEM module to establish the powder bed on the substrate plate. Subsequently, the WELD module was employed to simulate the molten pool dynamics, and the deposited track formation. The computational domain for the single-track deposition is displayed in Fig. 3. The mesh size of 4.5 µm was imposed for entire computational domain, which have been obtained from mesh convergence analysis as presented in Sect. 3. The space region over the powder bed layer was specified as atmospheric pressure. The initial temperature condition was set at a temperature of 473.15 K. Material employed as the metal particles, which have a spherical shape and substrate was Ti-6Al-4 V alloys. The particle size distributions (PSD) were d₁₀ $(12.03 \mu m)$, d_{50} $(21.38 \mu m)$, and d_{90} $(31.15 \mu m)$, respectively, which obtained from [40]. The packing fraction of powder bed was approximately 64%. The thermal-physical properties of Ti-6Al-4 V used in the calculation were given in Table 2 [48]. The thermal–physical properties with temperature dependent have been acquired from Ref. [49]. Table 3 illustrates operating parameters used for laser melting process. The laser spot size exploited in the study is 80 µm.



Fig. 3 The computational domain for single-track deposition. (Color figure online)

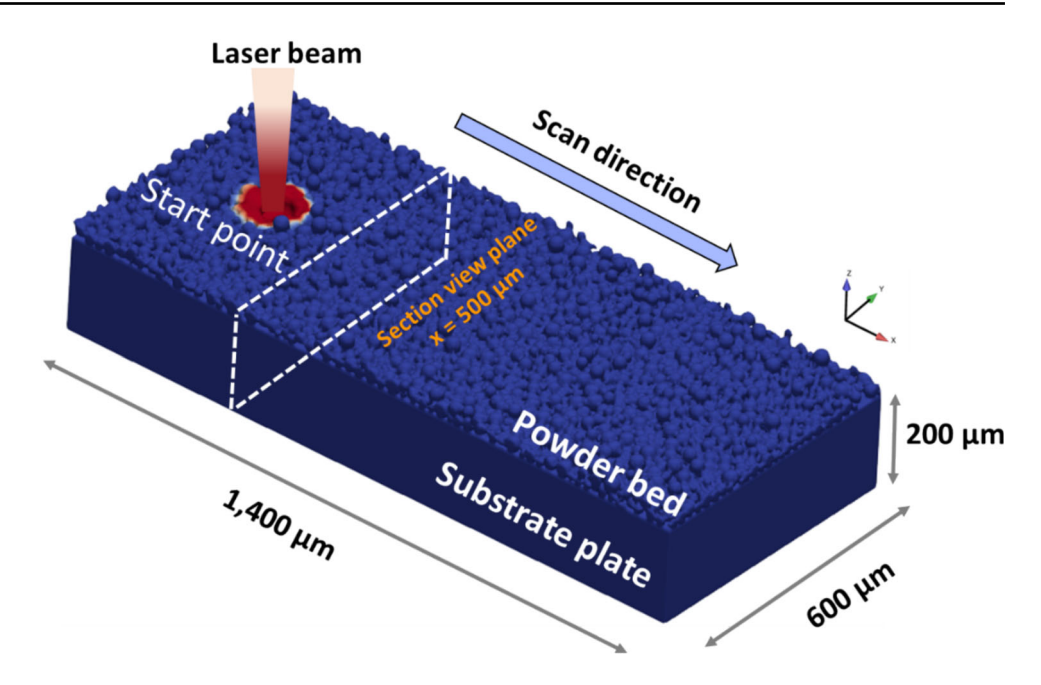
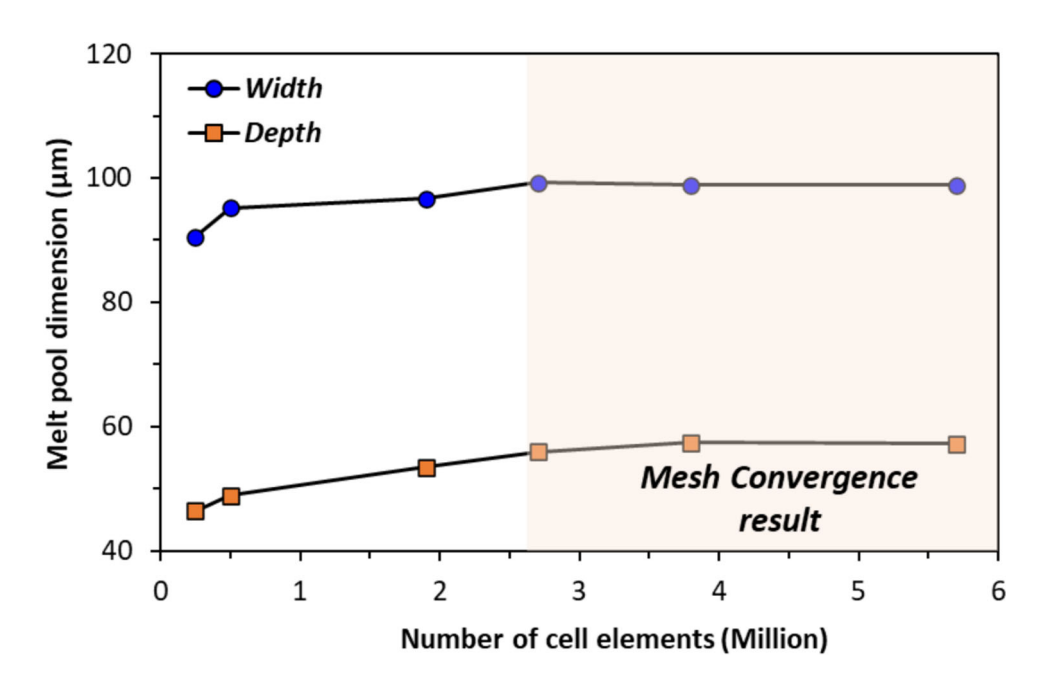


Table 3 Operating parameters used for laser melting process

Case studies	Designation	Laser power (W)	Scanning speed (mm/s)	LED (J/m)	Layer thickness (μm)	
1	A1	170	1,200	142	30	
2	A2	170	1,200	142	60	
3	A3	170	1,200	142	90	
4	B1	120	1,200	100	30	
5	B2	150	1,500	100	30	
6	В3	170	1,700	100	30	
7	C1	170	800	213	90	
8	C2	255	1,200	213	90	
9	C3	340	1,600	213	90	

Fig. 4 Mesh convergence result. (Color figure online)





3 Mesh convergence analysis

Mesh convergence analysis was initially examined to specify the suitable mesh size for the calculation. The mesh sizes with 3.5, 4, 4.5, 5, 8, and 10 μm were chosen for this analysis. The total number of mesh elements of each case were as follows: 5,882,400 elements, 3,937,500 elements, 2,771,321 elements, 2,016,000 elements, 498,750 elements, and 252,000 elements, respectively. The mesh convergence for the study was evaluated by investigating melt pool dimensions. From the analysis, it was found that the numerical result can converge at mesh sizes lesser than 4.5 μm as shown in Fig. 4. Hence, the mesh size of 4.5 μm was selected for the further simulation.

4 Results and discussion

4.1 Numerical model validation

The numerical results obtained were validated with the experimental results reported in the study of Kouprianoff et al. [40] to verify the accuracy and reliability of the numerical model. Figure 5 presents a comparison of dimensions of molten pool between the numerical and experimental results obtained from previous study [40] processed with a laser power of 170 W, scanning speed of 1,200 mm/s, and layer thickness of 30 μm . The numerical results were observed to be consistent with the experiment result. The simulation error of the molten pool width and depth are 2% and 7%, respectively. For this reason, the numerical model is suitable for further investigations in the present study as it provides reasonable numerical results.

4.2 Molten pool evolution with varying layer thickness

Figure 6 demonstrates the melt pool evolution at the transverse section view plane $x = 500 \mu m$ (see in Fig. 3) under three varying layer thicknesses processed with a laser power of 170 W and a scanning speed of 1,200 mm/s. At 390 µs, before the laser heat source reached the section view plane, the initial melting state of the powder bed can be observed. At a layer thickness of 30 µm, the powder bed was partially melted with the substrate plate, whereas at higher layer thicknesses of 60 μ m and 90 μ m, the powder bed was not melted deep enough to reach the substrate plate. As the laser source reached the section view plane at time = $420 \mu s$, the metal powder was fully melted and sufficiently penetrated in the substrate plate at layer thicknesses of 30 µm and 60 µm. Meanwhile, at the layer thickness of 90 μm, the powder bed was just partially melted with the substrate plate. This led to defect formation such as porosity and LOF [50]. Because

of the recoil pressure formation and surface tension at the surface of the molten pool, the molten metal was driven outwards from the center to the edges, and downward direction, resulting in the melt pool depression. Furthermore, the temperature distribution varies with layer thickness. At a layer thickness of 30 µm has a V-shaped profile and extends into the substrate as shown in Fig. 6a2. It can be gradually transformed to a U-shaped profile at higher layer thicknesses of 60 μm and 90 μm because the heat was dissipated slowly to form a uniform temperature distribution (see in Fig. 6 b2, and c2). By 470 µs, the molten pool in all cases has expanded both in depth and width due to heat accumulation. The melt pool evolution in all cases was in the initial solidification process when the laser source was moved away. Because the recoil pressure was released, changing the flow direction of molten metal from downwards to upwards was formed. This indicated that the gap of molten pool is starting to be filled [51, 52]. The surface morphology of molten pool presented a concave shape as displayed in Fig. 6a3–c3. At 520 µs, the temperature distribution profile of molten pool in all cases became U-shaped profile with uniform and round due to a more uniform heat dissipation as presented in Fig. 6a4-c4. The molten metal continuously upward flowed to fully replenish the gap of molten pool. This led to the surface of the melting pool being quite convex, and flat. The layer thickness of 30 µm case shows faster cooling, leading to quicker solidification. At the progress time of 750 µs, the molten pool was initiated to cooling stage. The temperature of the molten pool gradually diminished until below the solidus temperature of material. Consequently, the final solidified deposited track was generated [45, 53]. Moreover, the results indicated that the final molten pool at layer thickness of 30 and 60 µm manifested a semi-circular shape with convex surface morphology. This was mainly because of the Marangoni effect, and surface tension induced by the difference in temperature at the surface of the molten pool. In contrast, the final molten pool profile at layer thickness of 90 µm displayed a semi-circular shape with flat surface morphology due to a more uniform heat distribution as shown in Fig. 6a5–c5.

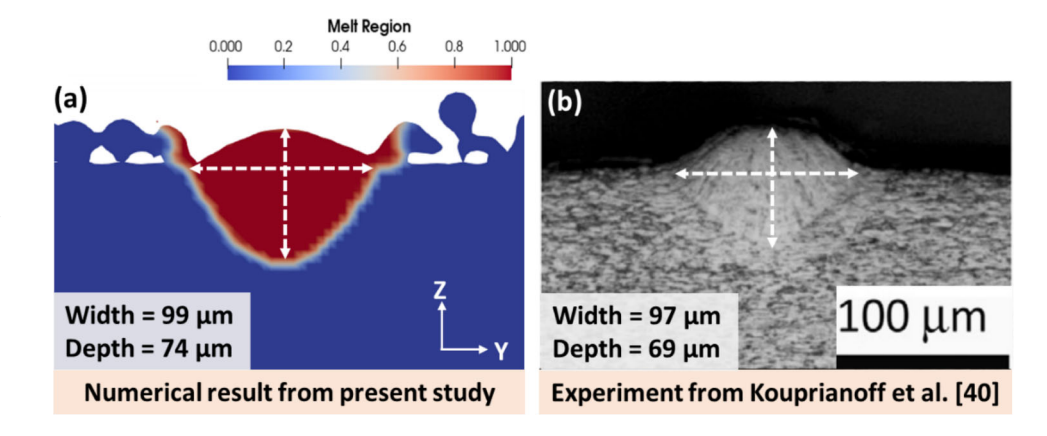
4.3 Formation of deposited track with varying layer thicknesses and LED parameter

4.3.1 Formation of deposited track with varying layer thicknesses

Figure 7 illustrates the formation of the deposited track with three varying layer thicknesses processed by laser power of 170 W and scanning speed of 1,200 mm/s, as LED of 142 J/m. The melt region is represented in red color, while the solid region is indicated in blue color. The numerical results revealed that the deposited track at layer thickness of



Fig. 5 A comparison of dimensions of melt pool between the numerical and experimental results obtained from previous study [40] processed with a laser power of 170 W, scanning speed of 1,200 mm/s, and layer thickness of 30 μ m. (Color figure online)



 $30 \mu m$ (A1) and $60 \mu m$ (A2) exhibited a near-circular shape of cross-section profile with convex surfaces, especially for the layer thickness of 30 µm layer due to faster heat dissipation. Conversely, increasing the layer thickness to 90 µm, the deposited track presented a flatter surface, semi-elliptical shape of cross-section profile with partial penetration into the substrate due to insufficient heat absorption and more laser reflection (see in Fig. 7c). As layer thickness increases, the molten pool morphology transformed from V-shaped to U-shaped because of more uniform heat dissipation. When observed from the longitudinal section across all cases of layer thickness, it was seen that the deposited track with continuous, and regular size can be formed. Based on the numerical results shown in Fig. 7, three different types of penetration depths (d_p) are observed: (1) excessive penetration depth at layer thickness of 30 µm, (2) optimal penetration depth at layer thickness of 60 µm, and (3) partial melting or insufficient penetration depth at layer thickness of 90 μm . This result can be confirmed by the d_p values of case A1, A2, and A3 presented in Table 4. Adjusting the LED, particularly for layer thickness of 30 μm and 90 μm, is essential to achieving optimal penetration. Nevertheless, the energy input parameter adjustment in the SLM process can highly impact the deposited track formation. Further analysis of energy input parameters was discussed in Sect. 4.3.2.

4.3.2 Formation of deposited track at layer thicknesses of 30 μm and 90 μm with LED parameter adjustment

Figures 8 and 9 illustrate the deposited track formation at layer thicknesses of 30 μm and 90 μm with the similar LED, but varied laser powers and scanning speeds. In this section, the laser power and scanning speed parameters were adjusted to achieve the optimal penetration depth at varying layer thickness of 30 μm (case B1-B3) and 90 μm (case C1-C3). The LED was reduced from 142 to 100 J/m for layer thicknesses of 30 μm and increased to 213 J/m for layer thickness of 90 μm . The simulation results indicated that deposited tracks with suitable penetration depth can be achieved at

layer thicknesses of 30 μ m and 90 μ m by adjusting the LED. Specifically, reducing the energy input from 142 to 100 J/m was effective for the 30 µm layer, while increasing the energy input to 213 J/m was necessary for the 90 µm layer. Nevertheless, the adjustment of LED significantly influenced the formation, dimensions, and melting mode of the deposited tracks. In this study, three distinction conditions for LED adjustment are performed: (1) adjustment laser power with constant scanning speed constant (Case B1, and Case C2), (2) adjustment of both laser power, and scanning speed (Case B2, and Case C3), and (3) adjustment of scanning speed with constant laser power (Case B3, and Case C1). In case B1, decreasing laser power from 170 to 120 W generated the deposited track with a semi-circular shape, uniform, and continuous track as shown in Fig. 8a and b. In contrast, increasing scanning speed from 1,200 to 1,500 mm/s, and 1,700 mm/s in Case B2 and B3, the presence of a narrower deposited track with the occurrence of periodic humps (humping effect) was observed [54] as illustrated in Fig. 8c, d, e and f. The humping effect is caused by Plateau–Rayleigh instability, which induces a backward flow of molten metal, leading to the accumulation of material at the hump surface. The occurrence of humping effect negatively impacts surface quality of the asbuilt product, and binding defect formation with next powder bed layer [54].

At layer thickness of 90 μ m, reducing scanning speed to 800 mm/s in Case C1, exhibited a continuous track with high penetration depth, although with irregular spikes at the bottom, which attributes the change of keyhole depth (see in Fig. 9a, and b) due to the high interaction time between laser heat energy and powder bed. In case C2, and C3, with increased laser power from 170 to 255 W, and to 340 W created the deposited track with continuous, smooth surface, regular size, and high penetration depth due to the higher energy density as shown in Fig. 9c, d, e and f.



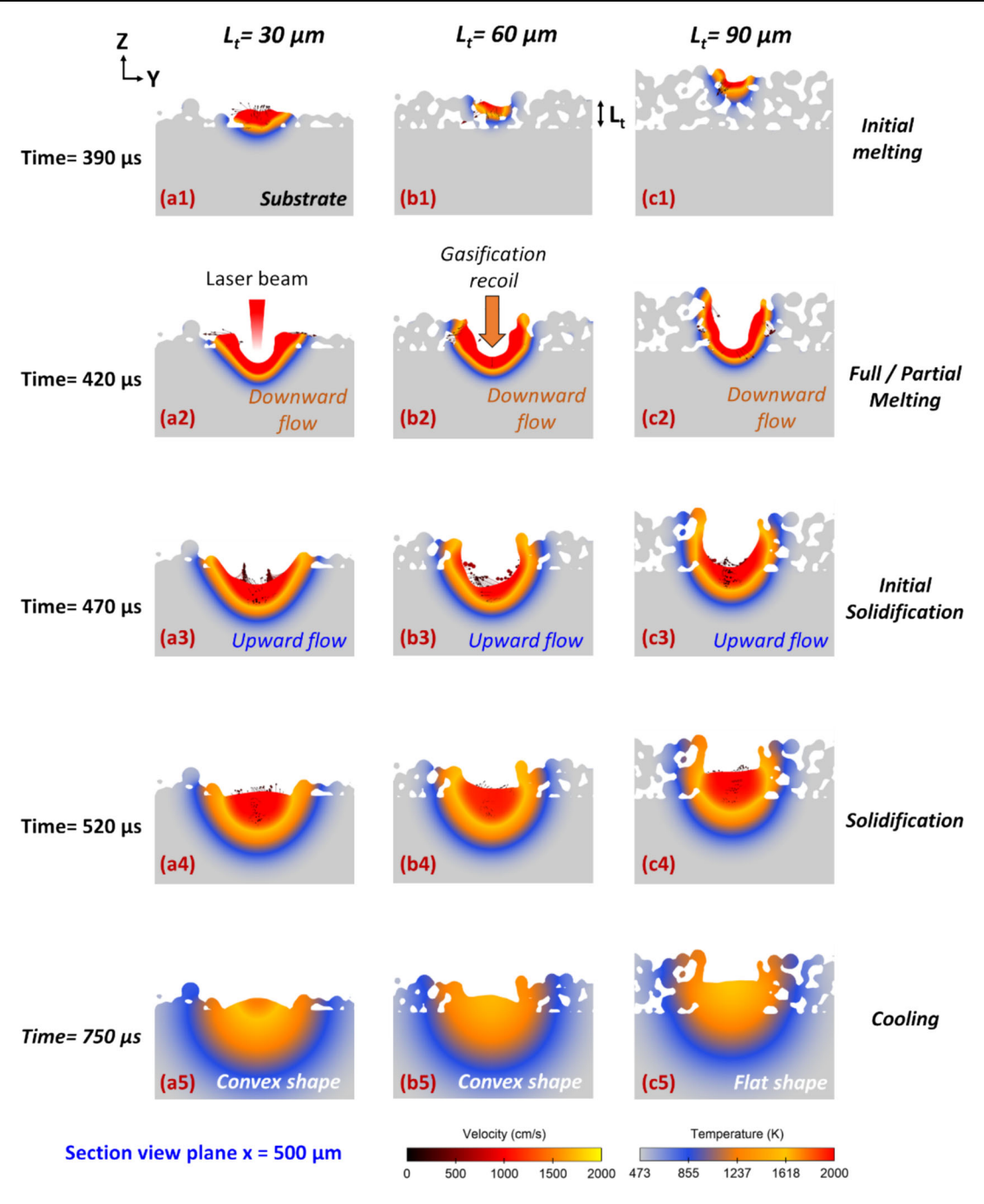


Fig. 6 Melt pool dynamics evolution under three varying layer thicknesses processed with a laser power of 170 W and scanning speed of 1,200 mm/s. (Color figure online)

4.3.3 Dimension of deposited track with varying layer thicknesses and LED parameter

Table 4 shows dimensions of deposited track with varying layer thickness and LED parameters adjustment. The dimensions of deposited track, namely width (w), depth (d), penetration depth (d_p) , and height (h) have been measured, and averaged at cross-sectional points located at 600 μ m,

700 μ m, and 800 μ m along scanning direction. The results showed that as layer thickness increases, penetration depth (d_p) tend to decrease, while the height of the molten pool (h) increases due to a greater number of melted powders. As the d_p of deposited track at layer thickness of 30 μ m, 60 μ m, and 90 μ m were 56 μ m, 46 μ m, and 22 μ m, respectively. The value indicated the difference of penetration depth was generated with varying layer thickness.



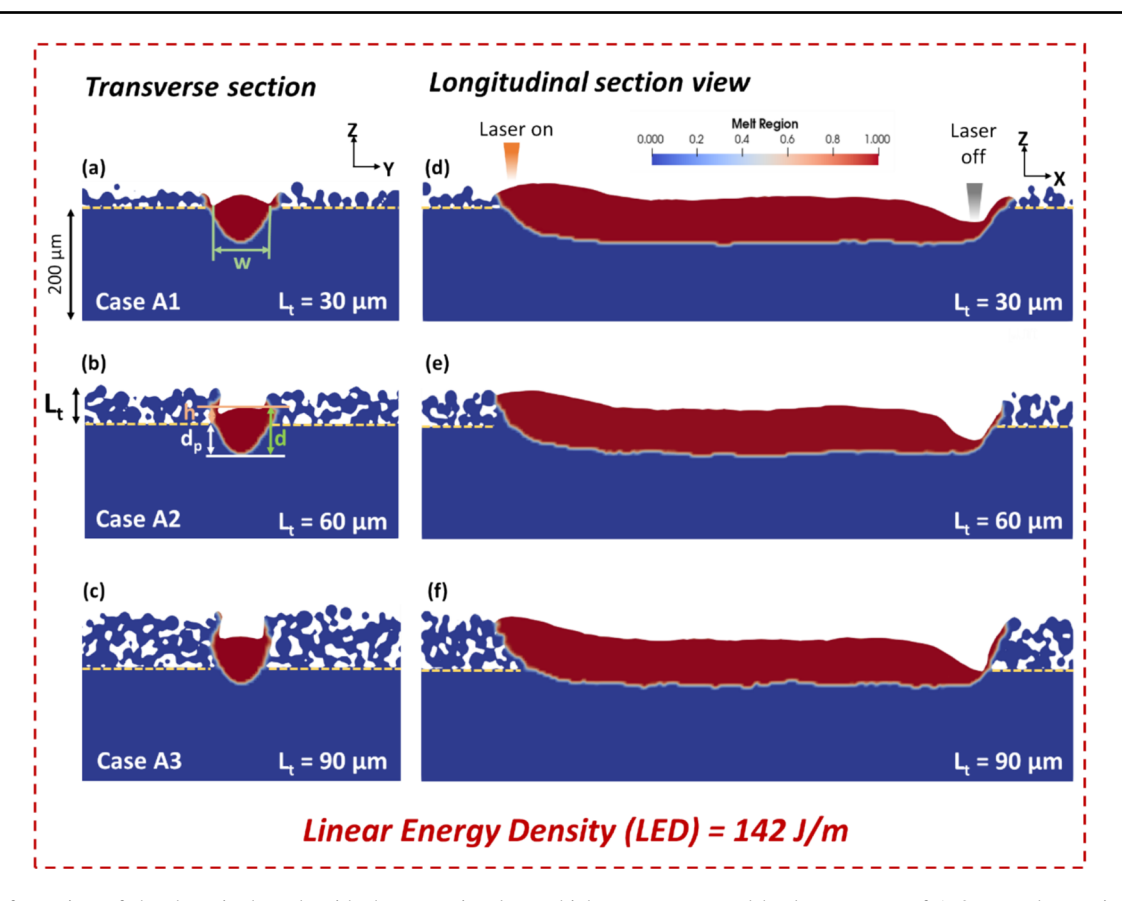


Fig. 7 The formation of the deposited track with three varying layer thicknesses processed by laser power of 170 W and scanning speed of 1,200 mm/s, as LED of 142 J/m. (Color figure online)

Table 4 Dimensions of deposited track with varying layer thickness and LED adjustment

Case studies	P(W)	V (mm/s)	LED (J/m)	$L_{t}\left(\mu m\right)$	$W\left(\mu m\right)$	$d_p \; (\mu m)$	H (µm)	$D\left(\mu m\right)$	d/w ratio
A1	170	1,200	142	30	99	56	19	74	0.75
A2	170	1,200	142	60	98	46	30	75	0.76
A3	170	1,200	142	90	98	22	53	74	0.77
B1	120	1,200	100	30	92	37	15	53	0.57
B2	150	1,500	100	30	87	39	17	56	0.64
В3	170	1,700	100	30	85	39	21	60	0.70
C1	170	800	213	90	88	61	44	105	1.19
C2	255	1,200	213	90	117	55	55	110	0.94
C3	340	1,600	213	90	109	45	62	107	0.98

Additionally, the dimensions of deposited at layer thickness of 30 μ m decreased with reducing LED to 100 J/m. For example, the dimensions, including w, d_p , and d was reduced from 99 μ m, 56 μ m, and 74 μ m (case A1) to 92 μ m, 37 μ m, and 53 μ m for case B1, 87 μ m, 39 μ m, and 56 μ m for case B2, and 85 μ m, 39 μ m, and 60 μ m for case B3. For the layer thickness of 90 μ m, the dimensions of deposited track enhanced when the LED was increased to 213 J/m. For example, the d_p , and d of deposited track was increased

from 22 μ m, and 74 μ m (Case A3) to 61 μ m, and 105 μ m for Case C1, 55 μ m, and 110 μ m for case C2, 45 μ m, and 107 μ m for case C3. However, the w of deposited track in case C1 reduced due to over energy density induced keyholing formation. The molten metal has an inward flow pattern. Meanwhile, the w of deposited track in case C2, and C3 was enlarged from 98 to 117 μ m, and 109 μ m. From the results, it can be observed that the adjustment of energy input parameters has a stronger effect on variation of deposited track



Fig. 8 Deposited track formation at layer thicknesses of $30 \mu m$ with the similar LED, but varied laser powers, and scanning speeds. (Color figure online)

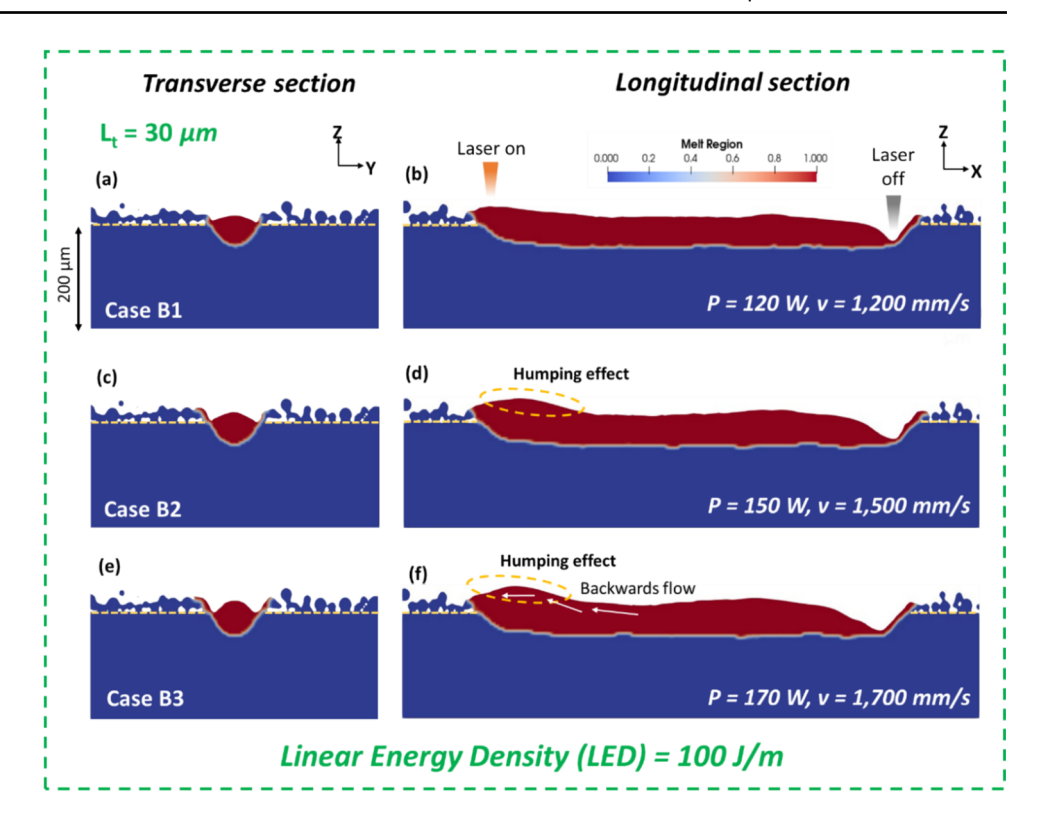
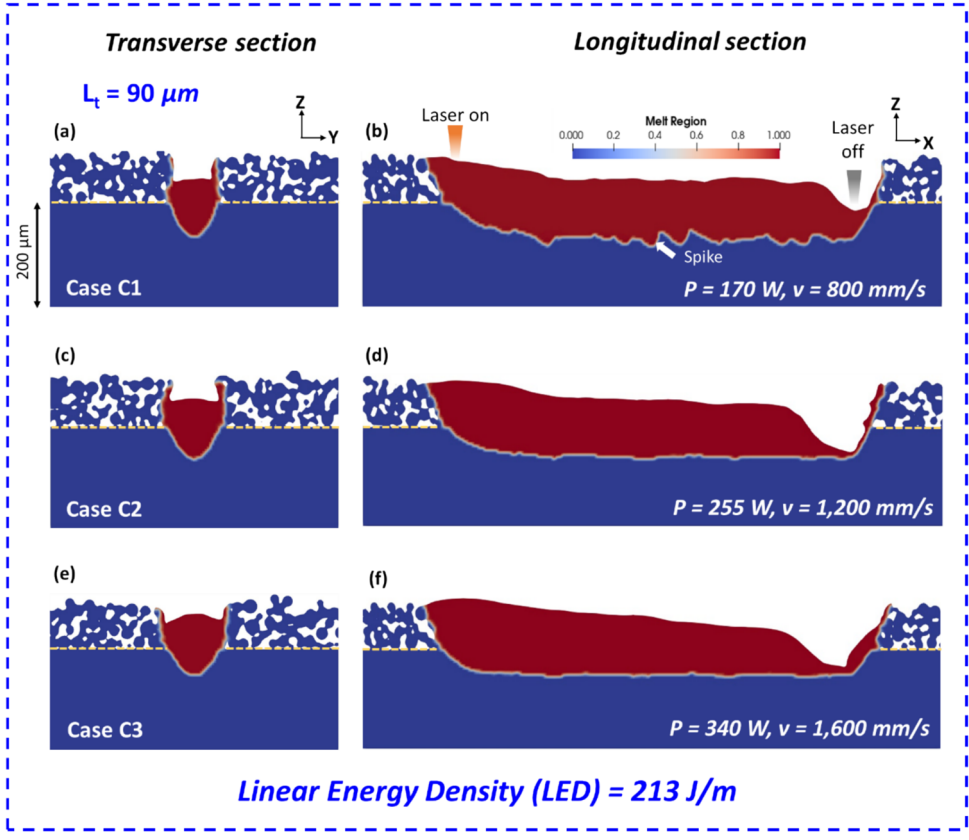


Fig. 9 Deposited track formation at layer thicknesses of $90~\mu m$ with the similar LED, but varied laser powers and scanning speeds. (Color figure online)





dimension at high layer thickness of 90 μ m than low layer thickness of 30 μ m because of process instability induced by energy density requirement at higher layer thickness.

To analyze the melting mode of molten pool, the depth to width (d/w) ratio parameter is generally employed to signify the melting modes of molten pool [55]. As mentioned in previous studies of Qi et al. [56] and Cullom et al. [57], the melting mode has been classified into three melting modes: (1) conduction mode (d/w ratio is less than 0.5), (2) transition mode (d/w ratio is between 0.5 and 1.1), and (3) keyhole mode (d/w ratio is over 1.1). Based on the simulation result, the d/w ratio of deposited track across all layer thickness 30, 60, and 90 μm case were around 0.75–0.77. This results in a transition mode. Meanwhile, the melting mode in cases B1-B3 had remained in transition mode while at layer thickness of 90 μm in Case C1-C3 varied between keyhole, and transition modes depending on the P, and v adjustments.

From the results shown earlier, it was noted that the adjustment of laser power at scanning speed constant condition is effective for achieving a desirable deposited track at layer thickness of 30 μm . On the other hand, the adjustment of the laser scanning speed condition at layer thickness of 30 μm , it will result in more undesirable deposited track formation. At layer thickness of 90 μm , the adjustment of laser power at scanning speed constant condition, and the adjustment of both laser power, and scanning speed condition is effective, and providing the potential to acquire the desirable deposited track.

4.4 Impact of process parameters on surface sinkage induced by the shrinkage of deposited track

Figure 10 displays melt pool depth and surface sinkage, and the sinkage percentage compared to the initial layer thickness of deposited tracks with varying layer thickness and LED parameters adjustment. The results showed that layer thicknesses, and LED parameters adjustment play a vital role in the surface sinkage of deposited tracks. The surface sinkage tends to increase as layer thickness increases under constant laser power of 170 W, scanning speed of 1200 mm/s, and a LED of 142 J/m due to the greater uniform heat distribution and higher thermal gradients. The surface sinkage increased from 11 µm for the 30 µm layer thickness to 31 µm, for the layer thickness 60 μ m, and to 37 μ m for the 90 μ m. Furthermore, the sinkage percentage (S_p) compared to the initial layer thickness was 38% for the 30 µm (case A1), 51% for the 60 μ m (case A2), and 41% for the 90 μ m (case A3). The 60 µm layer thickness case manifested the highest shrinkage percentage, likely due to more uniform heat distribution and controlled solidification. Due to higher thermal gradient, and uneven cooling rate, higher layer thickness tends to experience high shrinkage. This can result in the LOF defect in subsequent layer. Conversely, low layer thickness has lower shrinkage due to more efficient heat dissipation; however, the building rate is lower.

Moreover, the LED variation also affects surface sinkage across different layer thicknesses. At a lower layer thickness of 30 µm, the reduction in LED from 142 (case A1) to 100 J/m (case B1-B3) does not significantly impact surface sinkage compared to case A1. For example, reducing LED to 100 J/m, the surface sinkage of deposited track increased from 11 to 15 µm for case B1, and 13 µm for case B2. However, the surface sinkage was decreased to 9 µm for case B3. The S_p compared to the initial layer thickness of cases B1, B2, and B3 were 49%, 44%, and 31%, respectively. The highest surface sinkage of deposited track was created in case B1, which reduces the laser power maintaining a constant scanning speed. On the other hand, case B3, which used the highest scanning speed, showed the lowest surface sinkage among the three cases. This was due to an increase in scanning speed shortening the interaction time between the laser source and the powder bed, resulting in even less energy absorption, and consequently, reduced surface sinkage.

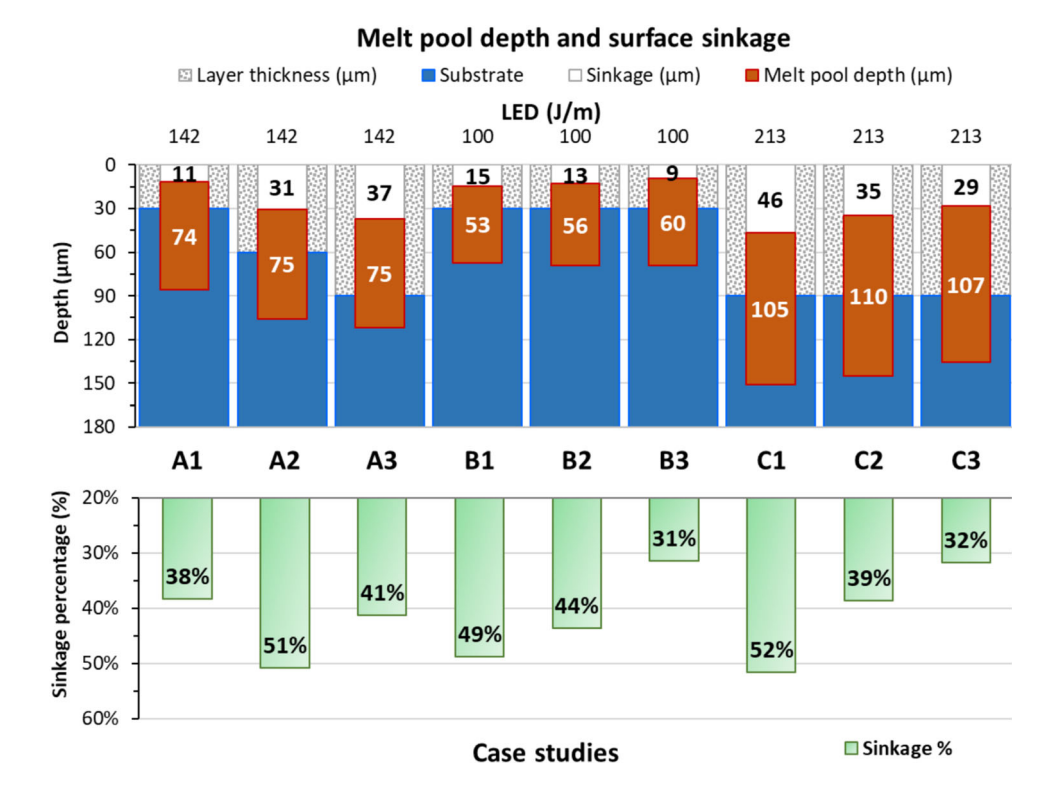
At the higher layer thickness of 90 µm, increasing LED from 142 (Case A3) to 213 J/m (Case C1-C3) highlighted that higher LED generally result in variation of surface sinkage due to deeper and larger molten pools that contract significantly upon cooling. For example, increasing LED to 213 J/m, the surface sinkage of deposited track significantly increased from 37 to 46 µm for case C1, while the surface sinkage was slightly decreased to 35 µm for case C2. Nevertheless, the surface sinkage was dramatically reduced to 29 μ m for case C3. The S_p compared to the initial layer thickness of cases C1, C2, and C3 were 52%, 39%, and 32%, respectively. With the higher LED and low scanning speed providing for a longer interaction time between the laser source and the powder bed, the deposited track with the highest d_p was generated, which has significant energy absorption, leading to the higher surface sinkage as the molten pool solidifies and contracts. As an increase in laser power under constant scanning speed of 1,200 mm/s in case C2, the energy density is sufficient to fully melt the powder to create a larger molten volume, nevertheless the faster scanning speed compared to case C1 slightly mitigates the extent of surface sinkage. Meanwhile, with the highest laser power and scanning speed, which reduces the interaction time, surface sinkage dramatically reduced compared to case C1 due to the faster cooling of molten pool. Effective control of shrinkage and deposited track depth (d) is important for producing defect-free components.

5 Conclusions

The research study implemented multi-physics simulation to investigate the deposited track formation, and surface sinkage



Fig. 10 Melt pool depth and surface sinkage and the sinkage percentage compared to the initial layer thickness of deposited track with varying layer thickness and LED parameters adjustment. (Color figure online)



induced by shrinkage during solidification with varying layer thicknesses, and the LED parameters in the SLM process of Ti-6Al-4 V alloy. The following findings in this study were acquired:

- The layer thickness significantly influences temperature distribution shaped profile, and molten pool shape. As layer thickness increases, the temperature distribution shaped profile transforms from a V-shaped to U-shaped and flat surface morphology of molten pool due to more uniform heat distribution.
- 2. The LED parameters adjustment plays a significant role on the deposited track formation, and surface sinkage. Reduction of LED parameters at lower layer thickness promoted uniform deposited track, but also led to humping effect. Conversely, increasing LED at higher layer thicknesses enhanced penetration depth but also led to potential keyholing, and increased surface sinkage.
- 3. Results showed that the adjusting LED parameters have an impact on the melting modes of molten pool at high layer thickness. At low layer thickness, when the LED was decreased from 142 to 100 J/m, the melting mode of deposited track remained in transition mode, Meanwhile, at high layer thickness, when the LED was increased from 142 to 213 J/m, the melting modes varied between keyhole, and transition modes depending on the laser power, and scanning speed adjustments.

4. Surface sinkage, which was driven by shrinkage during solidification, was found to be more pronounced with higher layer thicknesses. Increased LED at high layer thickness can either increase or decrease surface sinkage due to the change in melting mode. The results indicated the need to carefully balance energy input to manage surface sinkage while maintaining sufficient and good metallurgical bonding and dimensional accuracy.

This study is primarily focusing on the deposited track formation and surface sinkage of deposited track. However, the components in the SLM process are commonly created in a layer-by-layer addition. Therefore, the good overlap with adjacent solidified track, and sufficient overlap depth between deposited track in preceding layer and the deposited track in further layer is desirable to produce the build part with good quality, and defect free. Therefore, the study of process parameters impact on multi-tracks formation, multi-layer formation, surface sinkage, and defects generation is a significant research issue of our further study.

Acknowledgements This work was supported by National Research Council of Thailand and King Mongkut's University of Technology North Bangkok [grant numbers N42A650321].

Funding National Research Council of Thailand and King Mongkut's University of Technology North Bangkok, N42A650321, Pruet Kowitwarangkul

Data availability The data that support the findings of this study are available from the corresponding author upon reasonable request.



Declarations

Conflict of interest Conflict of interest The authors declare that they have no conflict of interest.

References

- Abd-Elaziem W, Elkatatny S, Abd-Elaziem AE, Khedr M, Abd Elbaky MA, Hassan MA, Abu-Okail M, Mohammed M, Järvenpää A, Allam T, Hamada A (2022) On the current research progress of metallic materials fabricated by laser powder bed fusion process: a review. J Mater Res Technol 20:681–707
- Wang J, Zhu R, Liu Y, Zhang L (2023) Understanding melt pool characteristics in laser powder bed fusion: an overview of singleand multi-track melt pools for process optimization. Adv Powder Mater 2:100137. https://doi.org/10.1016/j.apmate.2023.100137
- Nabavi SF, Farshidianfar A, Dalir H (2025) Comprehensive review: Advancements in modeling geometrical and mechanical characteristics of laser powder bed fusion process. Opt Laser Technol 180:111480
- Sefene EM (2022) State-of-the-art of selective laser melting process: a comprehensive review. J Manuf Syst 63:250–274
- Oliveira JP, LaLonde AD, Ma J (2020) Processing parameters in laser powder bed fusion metal additive manufacturing. Mater Des 193:108762. https://doi.org/10.1016/j.matdes.2020.108762
- Shi X, Ma S, Liu C, Chen C, Wu Q, Chen X, Lu J (2016) Performance of high layer thickness in selective laser melting of Ti6Al4V. Mater 9:975. https://doi.org/10.3390/ma9120975
- Hyer HC, Petrie CM (2022) Effect of powder layer thickness on the microstructural development of additively manufactured SS316. J Manuf Process 76:666–674. https://doi.org/10.1016/j.jm apro.2022.02.047
- Shi X, Yan C, Feng W, Zhang Y, Leng Z (2020) Effect of high layer thickness on surface quality and defect behavior of Ti-6Al-4V fabricated by selective laser melting. Opt Laser Technol 132:106471. https://doi.org/10.1016/j.optlastec.2020.106471
- Vilardell AM, Yadroitsev I, Yadroitsava I, Albu M, Takata N, Kobashi M, Krakhmalev P, Kouprianoff D, Kothleitner G, Plessis AD (2020) Manufacturing and characterization of in-situ alloyed Ti6Al4V(ELI)-3 at.% Cu by laser powder bed fusion. Addit Manuf 36:101436. https://doi.org/10.1016/j.addma.2020.101436
- Yadroitsev I, Yadroitsava I, Plessis AD, MacDonald E (2021) Fundamentals of laser powder bed fusion of metals. Elsevier, Amsterdam
- Bagasol AJI, Parivendhan G, Ivankovic A, Dowling DP (2024) Ti-6Al-4V alloy printing — correlations between experimental and numerical modelling melt pool data. Int J Adv Manuf Technol 133:3603–3617. https://doi.org/10.1007/s00170-024-13979-w
- Bayat M, Dong W, Thorborg J, To AC, Hattel JH (2021) A review of multi-scale and multi-physics simulations of metal additive manufacturing processes with focus on modeling strategies. Addit Manuf 47:102278. https://doi.org/10.1016/j.addma.2021.102278
- Cook PS, Murphy AB (2020) Simulation of melt pool behaviour during additive manufacturing: underlying physics and progress. Addit Manuf 31:100909. https://doi.org/10.1016/j.addma.2019.10 0909
- Thongpron R, Ninpetch P, Chalermkarnnon P, Kowitwarangkul P (2024) Effect of hatch spacing in selective laser melting process of Ti-6Al-4V alloy on finished surface roughness: a computational study. J Met Mater Miner 34:1861. https://doi.org/10.55713/ jmmm.v34i3.1861

- Wang X, Lu Q, Zhang P, Yan H, Shi H, Sun T, Zhou K, Chen K (2024) A review on the simulation of selective laser melting AlSi10Mg. Opt Laser Technol 174:110500. https://doi.org/10.1016/j.optlastec.2023.110500
- Ninpetch P, Kowitwarangkul P, Mahathanabodee S, Chalermkarnnon P, Ratanadecho P (2020) A review of computer simulations of metal 3D printing. AIP Conf Proc 2279:050002-1–050002-24. https://doi.org/10.1063/5.0022974
- Katagiri J, Kusano M, Nomoto S, Watanabe M (2023) Influence of recoil pressure, mushy zone flow resistance and reflectivity on melt pool shape in laser powder bed fusion simulation. Case Stud Therm Eng 50:103477. https://doi.org/10.1016/j.csite.2023.103477
- Ninpetch P, Chalermkarnnon P, Kowitwarangkul P (2023) Multiphysics simulation of thermal-fluid behavior in laser powder bed fusion of H13 steel: influence of layer thickness and energy input.
 Met Mater Int 29:536–551. https://doi.org/10.1007/s12540-022-01239-z
- Panwisawas C, Qiu C, Anderson MJ, Sovani Y, Turner RP, Attallah MM, Brooks JW, Basoalto HC (2017) Mesoscale modelling of selective laser melting: thermal fluid dynamics and microstructural evolution. Comput Mater Sci 126:479–490. https://doi.org/ 10.1016/j.commatsci.2016.10.011
- Chen D, Li G, Wang P, Zeng Z, Tang Y (2023) Numerical simulation of melt pool size and flow evolution for laser powder bed fusion of powder grade Ti6Al4V. Finite Elem Anal Des 223:103971. https://doi.org/10.1016/j.finel.2023.103971
- Liu S, Shin YC (2019) Additive manufacturing of Ti6Al4V alloy: a review. Mater Des 164:107552. https://doi.org/10.1016/j.matdes. 2018.107552
- Shipley H, McDonnell D, Culleton M, Coull R, Lupoi R, O'Donnell G, Trimble D (2018) Optimisation of process parameters to address fundamental challenges during selective laser melting of Ti-6Al-4V: a review. Int J Mach Tools Manuf 128:1–20. https://doi.org/10.1016/j.ijmachtools.2018.01.003
- Ge W, Fuh JYH, Na SJ (2021) Numerical modelling of keyhole formation in selective laser melting of Ti6Al4V. J Manuf Process 62:646–654. https://doi.org/10.1016/j.jmapro.2021.01.005
- Yang X, Li Y, Li B (2023) Formation mechanisms of lack of fusion and keyhole-induced pore defects in laser powder bed fusion process: a numerical study. Int J Therm Sci 188:108221. https://doi. org/10.1016/j.ijthermalsci.2023.108221
- Ji X, Zhang S, Wang Y, Liang SY (2022) Effect of thermal-fluidic transport on the temperature distribution and the melt pool in laser powder bed fusion of Ti6Al4V. Opt Laser Technol 156:108587. https://doi.org/10.1016/j.optlastec.2022.108587
- Liu B, Fang G, Lei L, Yan X (2022) Predicting the porosity defects in selective laser melting (SLM) by molten pool geometry. Int J Mech Sci 228:107478. https://doi.org/10.1016/j.ijmecsci.2022.10 7478
- Liu B, Fang G, Lei L (2021) An analytical model for rapid predicting molten pool geometry of selective laser melting (SLM). Appl Math Model 92:505–524. https://doi.org/10.1016/j.apm.2020.11027
- Mirkoohi E, Ning J, Bocchini P, Fergani O, Chiang KN, Liang SY (2018) Thermal modeling of temperature distribution in metal additive manufacturing considering effects of build layers, latent heat, and temperature-sensitivity of material properties. JMMP 2:63. https://doi.org/10.3390/jmmp2030063
- Ansari MJ, Nguyen DS, Park HS (2019) Investigation of SLM process in terms of temperature distribution and melting pool size: modeling and experimental approaches. Materials 12:1272. https://doi.org/10.3390/ma12081272
- Xiang Z, Yin M, Dong G, Mei X, Yin G (2018) Modeling of the thermal physical process and study on the reliability of linear energy density for selective laser melting. Results Phys 9:939–946. https://doi.org/10.1016/j.rinp.2018.03.047



- Dai D, Gu D, Ge Q, Ma C, Shi X, Zhang H (2020) Thermodynamics of molten pool predicted by computational fluid dynamics in selective laser melting of Ti6Al4V: surface morphology evolution and densification behavior. Comput Model Eng Sci 124:1085–1098. https://doi.org/10.32604/cmes.2020.010927
- Xiang Y, Zhang S, Wei Z, Li J, Wei P, Chen Z, Yang L, Jiang L (2018) Forming and defect analysis for single track scanning in selective laser melting of Ti6Al4V. Appl Phys A 124:685. https://doi.org/10.1007/s00339-018-2056-9
- Yao XX, Zhang Z (2022) Laser-particle interaction-based heat source model of laser powder bed fusion additive manufacturing. Opt Laser Technol 155:108402. https://doi.org/10.1016/j.optlastec. 2022.108402
- Qian Y, Yan W, Lin F (2019) Data mining for mesoscopic simulation of electron beam selective melting. Eng 5:746–754. https://doi.org/10.1016/j.eng.2019.06.006
- Bogdanova M, Chernyshikhin S, Zakirov A, Zotov B, Fedorenko L, Belousov S, Perepelkina A, Korneev B, Lyange M, Pelevin I, Iskandarova I, Dzidziguri E, Potapkin B, Gromov A (2024) Mesoscale simulation of laser powder bed fusion with an increased layer thickness for AlSi10Mg alloy. JMMP 8:7. https://doi.org/10.3390/jmmp 8010007
- Liu B, Fang G, Lei L, Liu W (2022) Experimental and numerical exploration of defocusing in laser powder bed fusion (LPBF) as an effective processing parameter. Opt Laser Technol 149:107846. https://doi.org/10.1016/j.optlastec.2022.107846
- Rauniyar SK, Chou K (2019) Melt pool analysis and mesoscale simulation of laser powder bed fusion process (L-PBF) with Ti-6Al-4V powder particles. JOM 71:938–945. https://doi.org/10. 1007/s11837-018-3208-2
- Chia HY, Wang L, Yan W (2023) Influence of oxygen content on melt pool dynamics in metal additive manufacturing: high-fidelity modeling with experimental validation. Acta Mater 249:118824. https://doi.org/10.1016/j.actamat.2023.118824
- 39. Wu Y, Wu Q, Li M, Wang J, Yao D, An X, Fu H, Zhang H, Yang X, Zou Q, Li S, Ji H, Zhang X (2023) Numerical investigation on effects of operating conditions and final dimension predictions in laser powder bed fusion of molybdenum. Addit Manuf 76:103783. https://doi.org/10.1016/j.addma.2023.103783
- Kouprianoff D, Yadroitsava I, Du Plessis A, Luwes N, Yadroitsev I (2021) Monitoring of laser powder bed fusion by acoustic emission: investigation of single tracks and layers. Front Mech Eng 7:678076. https://doi.org/10.3389/fmech.2021.678076
- Wang W, Lin W, Yang R, Wu Y, Li J, Zhang Z, Zhai Z (2022) Mesoscopic evolution of molten pool during selective laser melting of superalloy Inconel 738 at elevating preheating temperature. Mater Des 213:110355. https://doi.org/10.1016/j.matdes.2021.110355
- Lee YS, Zhang W (2016) Modeling of heat transfer, fluid flow and solidification microstructure of nickel-base superalloy fabricated by laser powder bed fusion. Addit Manuf 12:178–188. https://doi. org/10.1016/j.addma.2016.05.003
- Zhang Y, Fang X, Zhang W, Guo W, Wang Z, Zhao J (2023) Molten pool flow behavior and influencing factors in electron beam selective melting of IN738 superalloy. Front Mater 10:1211648. https:// doi.org/10.3389/fmats.2023.1211648
- Cheng B, Loeber L, Willeck H, Hartel U, Tuffile C (2019) Computational investigation of melt pool process dynamics and pore formation in laser powder bed fusion. J Mater Eng Perform 28:6565–6578. https://doi.org/10.1007/s11665-019-04435-y
- Wu YC, San CH, Chang CH, Lin HJ, Marwan R, Baba S, Hwang WS (2018) Numerical modeling of melt-pool behavior in selective laser melting with random powder distribution and experimental validation. J Mater Process Technol 254:72–78. https://doi.org/10. 1016/j.jmatprotec.2017.11.032

- Wu Q, Qiao C, Wu Y, Liu Z, Li X, Wang J, An X, Huang A, Lim CVS (2023) Numerical investigation on the reuse of recycled powders in powder bed fusion additive manufacturing. Addit Manuf 77:103821. https://doi.org/10.1016/j.addma.2023.103821
- Ge W, Han S, Na SJ, Fuh JYH (2021) Numerical modelling of surface morphology in selective laser melting. Comput Mater Sci 186:110062. https://doi.org/10.1016/j.commatsci.2020.110062
- Wu C, Zafar MQ, Zhao H, Wang Y, Schöler C, Heinigk C, Nießen M, Schulz W (2021) Multi-physics modeling of side roughness generation mechanisms in powder bed fusion. Addit Manuf 47:102274. https://doi.org/10.1016/j.addma.2021.102274
- Mills KC (2002) Recommended Values of Thermophysical Properties for Selected Commercial Alloys. Woodhead Publishing, England
- Cao L (2019) Numerical simulation of the impact of laying powder on selective laser melting single-pass formation. Int J Heat Mass Transf 141:1036–1048. https://doi.org/10.1016/j.ijheatmass transfer.2019.07.053
- Zhang T, Li H, Liu S, Shen S, Xie H, Shi W, Zhang G, Shen B, Chen L, Xiao B, Wei M (2019) Evolution of molten pool during selective laser melting of Ti–6Al–4V. J Phys D Appl Phys 52:055302. https://doi.org/10.1088/1361-6463/aaee04
- Chen X, Mu W, Xu X, Liu W, Huang L, Li H (2021) Numerical analysis of double track formation for selective laser melting of 316L stainless steel. Appl Phys A 127:586. https://doi.org/10.1007/ s00339-021-04728-x
- Ninpetch P, Kowitwarangkul P, Mahathanabodee S, Chalermkarnnon P, Rattanadecho P (2021) Computational investigation of thermal behavior and molten metal flow with moving laser heat source for selective laser melting process. Case Stud Therm Eng 24:100860. https://doi.org/10.1016/j.csite.2021.100860
- Tang C, Le KQ, Wong CH (2020) Physics of humping formation in laser powder bed fusion. Int J Heat Mass Transf 149:119172. https://doi.org/10.1016/j.ijheatmasstransfer.2019.119172
- 55. Xu Y, Zhang Y, Li X, Zhong Y, Lin K, Liao B, Guo X, Yuan C, Zhang S (2024) Single-track investigation of additively manufactured mold steel with larger layer thickness processing: track morphology, melt pool characteristics and defects. Opt Laser Technol 171:110378. https://doi.org/10.1016/j.optlastec.2023.110378
- Qi T, Zhu H, Zhang H, Yin J, Ke L, Zeng X (2017) Selective laser melting of Al7050 powder: melting mode transition and comparison of the characteristics between the keyhole and conduction mode. Mater Des 135:257–266. https://doi.org/10.1016/j.matdes. 2017.09.014
- Cullom T, Lough C, Altese N, Bristow D, Landers R, Brown B, Hartwig T, Barnard A, Blough J, Johnson K, Kinzel E (2021) Frequency domain measurements of melt pool recoil force using modal analysis. Sci Rep. https://doi.org/10.1038/s41598-021-90423-z

Publisher's Note Springer Nature remains neutral with regard to jurisdictional claims in published maps and institutional affiliations.

Springer Nature or its licensor (e.g. a society or other partner) holds exclusive rights to this article under a publishing agreement with the author(s) or other rightsholder(s); author self-archiving of the accepted manuscript version of this article is solely governed by the terms of such publishing agreement and applicable law.

